

Redshifted absorption lines from an isolated neutron star

Sergio Campana (✉ sergio.campana@brera.inaf.it)

INAF <https://orcid.org/0000-0001-6278-1576>

Letter

Keywords: isolated neutron star, redshifted absorption lines, blackbody spectrum, atmospheric composition

Posted Date: September 21st, 2020

DOI: <https://doi.org/10.21203/rs.3.rs-77389/v1>

License:  This work is licensed under a Creative Commons Attribution 4.0 International License.

[Read Full License](#)

Redshifted absorption lines from an isolated neutron star

Sergio Campana¹

¹*INAF-Osservatorio astronomico di Brera, Via Bianchi 46, I-23807, Merate (LC), Italy*

The solid crust constituting the outer layers of a hot neutron star is wrapped by an mm-to-cm thin atmosphere. Even if the atmosphere is so thin, it substantially affects the blackbody spectrum emitted by the surface, resulting in an overall hardening of the emitted spectrum¹. The composition of the atmosphere has so far remained elusive. Several narrow absorption features have been detected and interpreted as arising from proton (or electron) resonant cyclotron absorption in the neutron star magnetic field²⁻⁴. Apart from these, for a Hydrogen atmosphere no spectral features are expected, whereas when it is polluted with metals, absorption features start appearing in soft X-ray spectra^{5,6}. Absorption edges and features have been possibly observed during thermonuclear explosions onto the neutron star surface^{7,8}. Isolated neutron stars represent a breeding ground where to look for absorption features, thanks to their simple X-ray spectra. Here we report on the detection of redshifted Nitrogen and Oxygen absorption features from the closest and brightest isolated neutron star. The lines are ~ 50 eV wide and their intensity is incompatible from originating in the interstellar path to the neutron star. Lines are redshifted by a common gravitational redshift of $z_g = 0.216 \pm 0.004$.

The magnificent seven is a group of nearby, cooling, relatively young, and isolated neutron stars^{3,9}. Their X-ray spectra are very simple, consisting of a cooling thermal component.

The brightest, closest, and first discovered samurai is RX J1856.5–3754 (RXJ1856 hereafter). It was discovered in the *ROSAT* all-sky survey¹⁰ and deeply investigated at all wavelengths. RXJ1856 lies at 123_{-15}^{+11} pc¹¹, spins at 7.055 s¹² (even if with a small pulsed fraction of $\sim 1.2\%$ in the 0.15-1.2 keV energy band, which made difficult its discovery), and has an inferred dipolar magnetic field at the equator of $\sim 2 \times 10^{13}$ G¹³. The *ROSAT* X-ray spectrum can be fitted with a simple blackbody of $kT_{\text{eff}} \sim 57$ eV and with a very low Galactic absorption $N_H \sim 10^{20}$ cm⁻², due to its proximity¹⁴.

Larger telescopes provided more photons but also more problems. The best modelling has been achieved with a thin, magnetic, partially ionised hydrogen atmosphere on top of a condensed surface using *Chandra* grating data¹⁵. The temperature is even lower $kT_{\text{eff}} \sim 45$ eV and the hydrogen atmosphere is partially ionised. With this model the authors indirectly estimated the gravitational redshift $z_g \sim 0.22$ (where $(1 + z_g) = 1/\sqrt{(1 - 2GM/Rc^2)}$, G is the gravitational constant; M and R are the neutron star mass and radius; and c is the speed of light). Deep *XMM-Newton* observations revealed that the spectrum collected with the pn instrument is position-dependent, being the source too bright not to hit the calibration accuracy. In this case, a successful modelling of the X-ray spectrum has been achieved with two blackbody components, one “hot” ($kT_{\text{eff}} \sim 62$ eV) with a small radius (~ 5 km) and one “cold” ($kT_{\text{eff}} \sim 39$ eV) consistent with the entire surface (~ 12 km)¹⁶. No absorption lines were detected in this study with an upper limit of ~ 6 eV on the equivalent width.

Due to its spectral stability and soft spectrum, RXJ1856 is often used as a calibration source for a number of X-ray instruments. *XMM-Newton* observed RXJ1856 42 times during its lifetime, collecting more than 2 Ms exposure. We focussed first on the high resolution in-

struments, namely the Reflection Grating Spectrometers (RGS¹⁷). After a standard filter and data extraction procedure (see Methods for more details), we obtained 2.31 Ms and 2.24 Ms exposures for the RGS1 and RGS2, respectively, comprising 0.38 Mcounts in the 0.324–0.8 keV energy range for the RGS1, and 0.33 Mcounts in the 0.332–0.5 plus 0.625–0.8 keV energy ranges (due to the failure of one CCD) for the RGS2. To complement these data, we also added *Chandra* Low Energy Transmission Grating Spectrometer (LETG¹⁸). We collected 0.61 Ms with the High Resolution Camera (HRC, 0.18 Mcounts in the 0.22–0.28 keV plus 0.32–0.8 keV energy range) and 0.25 Ms with the Advanced CCD Imaging Spectrometer (ACIS, 6 kcounts in the 0.22–0.28 keV plus 0.41–0.8 keV energy range). Given our interest in narrow absorption (or emission in principle) features, we do not focus too much on the overall continuum model: we just need to have a good fit of the continuum on top of which searching for lines. This has been achieved with an absorbed double blackbody model (a blackbody and a neutron star atmosphere model provides similar results). Given the superb statistics of our spectra, we leave the column density, blackbody temperatures and radii for each instrument to vary independently. We obtained broadly consistent results for each instrument (see Methods). A first iteration is then applied on the ungrouped spectra to get rid of small-width (< 1 eV, Gaussian sigma) absorption/emission lines, using Cash statistics to remove possible spurious features. We found a few of them. We then turned to χ^2 statistics grouping data to 10 (RGS1, RGS2), 300 (LETG-HRC), and 150 (LETG-ACIS) counts per energy bin (the higher grouping for the *Chandra* data is driven by the higher background and spectral resolution) and Churazov weighting scheme to use χ^2 statistics. We then added iteratively Gaussian lines (either with a positive or negative normalisation in the 0.25–0.8 keV energy range) until the variation in the χ^2 is more than 10. This turned out to be a very good prescription to identify high significance

lines (see Methods for more details).

We end up with two lines. The first line is at 411 ± 1 eV (errors are computed for $\Delta\chi^2 = 2.7$, equivalent to a 90% confidence level for one parameter of interest) and its inclusion in the fit produces a $\Delta\chi^2 = 46.2$. The line is structured and it is modelled with two Gaussians, one narrow 4 ± 2 eV wide and the other large 38 ± 10 eV wide. The equivalent width of the line is 4.2 ± 2.3 eV (3.5 eV and 0.6 eV for the large and narrow components, respectively). The second line is at 562 ± 10 eV ($\Delta\chi^2 = 30.2$), it is 32 ± 12 eV wide, and its equivalent width is 6.5 ± 2.2 eV. The identification of the two lines is not straightforward. The low energy line can be tentatively identified with NV Ly α (also known as K α , at 421.5 eV), only including a non-negligible redshift of ~ 0.03 , and the high energy line with OVI Ly α (at 563.1 eV) with no redshift (see Fig. 1). Line energy is not the only important quantity, however. Converting the line equivalent width to a, more physical, column density with a curve of growth analysis^{19,20}, one obtains very large values ($N_{\text{OVI}} \sim 5 \times 10^{17} \text{ cm}^{-2}$ and $N_{\text{NV}} \sim 3 \times 10^{17} \text{ cm}^{-2}$) for each element. This value has been computed entirely attributing the line width to the thermal broadening ($\sim 20,000 \text{ km s}^{-1}$), thus providing the lowest possible column density. Even assuming that these are the only atomic species, assuming Solar abundances²¹, one obtains equivalent column densities of $N_{\text{H}} \sim 10^{21} \text{ cm}^{-2}$ and $N_{\text{H}} \sim 4 \times 10^{21} \text{ cm}^{-2}$, respectively. These values are much larger than the observed equivalent column density along the line of sight to RXJ1856, which is a few 10^{20} cm^{-2} . This is true for any kind of material, diluted or compact, along the line of sight.

Weak absorption features have been observed in all the seven isolated neutron star, except of RX J1856: narrow features around 0.57 keV and 0.53 keV were observed in RX J0720.4–3125^{4,23} the second brightest isolated neutron star; RX J1605.3+3249 showed a broad absorp-

tion feature at 0.40 keV and a narrow feature at 0.57 keV^{24–26}; RX J1308.6+2127 showed an absorption feature at 0.53 keV in the co-added RGS spectra⁴. Phase dependent absorption features were observed in RX J0720.4–3125 and RX J1308.6+2127, and interpreted as proton cyclotron lines²⁷. Given the magnetic field of RXJ1856 ($\sim 2 \times 10^{13}$ G), this feature is expected to lie outside the relevant energy range (~ 0.06 keV for protons and ~ 120 keV for electrons). Using a model of a condensed iron surface, with a partially ionised thin hydrogen atmosphere a gravitational redshift of $z = 0.15$ and $z = 0.205$ has been indirectly estimated in RBS 1223 and RX J0720.4–3125, respectively^{28,29}.

The detection of absorption features close in energy to the ones reported here testifies that no calibration issues are present. These lines were usually interpreted either as arising from the hot interstellar medium or in a localised hot medium, possibly clumpy, along the line of sight. The observations of similar features in a number of isolated neutron stars make the second hypothesis untenable: the hot medium should have a large covering factor increasing too much the overall mass^{4,23}. The close distance to and the lack of detected features in RXJ1856 was indeed taken as a proof for the hot interstellar medium hypothesis⁴. Our line detection in the closest isolated neutron star (~ 120 pc) indicate instead that also this scenario has to be discarded, leaving only lines originating at the star surface and redshifted by gravity.

Following this line of reasoning, we are forced to attribute these lines to the atmosphere of the neutron star, where matter is not lacking, and the emission spectrum is produced. In this case, lines will be redshifted by the neutron star gravitational field and also the atmosphere temperature should be higher, allowing only for the highest ionisation species to be present. Thus, our line identification has to be changed. We consider the two H-like ions NVII Ly α (at

500.3 eV) and OVIII Ly α (at 653.6 eV). We fix the line energy and allow for the same (free) redshift of the lines. We also require that the two wide lines have the same width. We derived a comparable fit and a gravitational redshift $z_g = 0.216 \pm 0.004$. The Gaussian line with is $54.6^{+6.8}_{-5.7}$ eV. Considering the full width at a half maximum we obtain $\Delta\lambda/\lambda \sim 0.25$.

At this point we searched for a confirmation in the *XMM-Newton* pn data. As already stated, pn data suffer from calibration issues (when challenged with this huge number of counts, almost 6 millions) and the spectra are position dependent. Following Sartore et al.¹⁶, we identified five positions on the detector, extracted the relevant spectra and response files (see Methods). We then fit the data with an absorbed double blackbody model, finding four weak and broad absorption features. Two of them are consistent with those found in high resolution spectral data. The equivalent widths are still too large (~ 10 eV) to come from material along the line of sight. Looking for redshifted lines we tentatively identify NVII Ly α , NVII Ly β , OVIII Ly α , and OVIII Ly β , at a common redshift of $z_g = 0.224 \pm 0.015$. This value is consistent with the one derived from high resolution spectral data. Given the uncertainties in the position-dependent calibration of the pn detector, however, we consider this as an indirect confirmation of the results obtained with high resolution spectral data.

The value of z_g calls for standard values for the neutron star parameters: for a standard mass of $1.4 M_\odot$ we derive a radius of 12.8 ± 0.2 km or, for a 12 km radius a mass of $1.31 \pm 0.01 M_\odot$ (Fig. 2). This might indicate that magnetars are born with a mass somewhat lower than the canonical neutron star mass. Atmosphere models with a mixture of elements, as foreseen by our spectral fits, do not exist and should be developed to test in more depth our results. This can lead to derive directly from the fit the mass and radius of the neutron star. A 100 ks *Athena*

X-IFU observation will provide a $\sim 1\%$ error on the gravitational redshift and a comparable precision on the independent estimate of the neutron star mass and radius.

1. Yakovlev, D. G. & Pethick, C. J. Neutron Star Cooling. *Annu. Rev. Astron. Astrophys.* **42**, 169–210 (2004).
2. Bignami, G. F. *et al.* The magnetic field of an isolated neutron star from X-ray cyclotron absorption lines. *Nature* **423**, 725–727 (2003).
3. Haberl, F., The magnificent seven: magnetic fields and surface temperature distributions. *Ap&SS* **308**, 181–190 (2007).
4. Hohle, M. M. *et al.* Narrow absorption features in the co-added XMM-Newton RGS spectra of isolated neutron stars. *Mon. Not. R. Astron. Soc.* **419**, 1525–1536 (2018).
5. Ho, W. G. C. & Heinke, C. O. A neutron star with a carbon atmosphere in the Cassiopeia A supernova remnant. *Nature* **462**, 71–73 (2009).
6. Suleimanov, A., Potekhin, A. Y. & Werner, K. Models of magnetized neutron star atmospheres: thin atmospheres and partially ionized hydrogen atmospheres with vacuum polarization. *Astron. Astrophys.* **500**, 891–899 (2009).
7. Cottam, J., Paerels, F. & Mendez, M. Gravitationally redshifted absorption lines in the X-ray burst spectra of a neutron star. *Nature* **420**, 5154 (2002).
8. in t Zand, J. J. M. & Weinberg, N. N. Evidence of heavy-element ashes in thermonuclear X-ray bursts with photospheric superexpansion. *Astron. Astrophys.* **520**, A81 (2010).

9. Turolla, R., Isolated Neutron Stars: The Challenge of Simplicity. *Neutron Stars and Pulsars, Astrophysics and Space Science Library* **357**, 141 (2009).
10. Neuhaeuser, R. *et al.* On the X-ray position and deep optical imaging of the neutron star candidate RX J1856.5-3754. *Astron. Astrophys.* **318**, 43–46 (1997).
11. Walter, F. M. *et al.* Revisiting the Parallax of the Isolated Neutron Star RX J185635-3754 Using HST/ACS Imaging. *Astrophys. J.* **724**, 669–677 (2010).
12. Tiengo, A. & Mereghetti, S. XMM-Newton Discovery of 7 s Pulsations in the Isolated Neutron Star RX J1856.5-3754. *Astrophys. J.* **657**, L101–L104 (2007).
13. van Kerkwijk, M. H. & Kaplan, D. L. Timing the Nearby Isolated Neutron Star RX J1856.5-3754. *Astrophys. J.* **673**, L163 (2008).
14. Campana, S., Mereghetti, S. & Sidoli, L. Is RX J1856.5-3754 an old neutron star?. *Astron. Astrophys.* **320**, 783–786 (1997).
15. Ho, W. G. C. Constraining the geometry of the neutron star RX J1856.5-3754. *Mon. Not. R. Astron. Soc.* **380**, 71–77 (2007).
16. Sartore, N. *et al.* Spectral monitoring of RX J1856.5-3754 with XMM-Newton. Analysis of EPIC-pn data. *Astron. Astrophys.* **541**, A66 (2012).
17. den Herder, J. W. *et al.* The Reflection Grating Spectrometer on board XMM-Newton. *Astron. Astrophys.* **365**, L7–L17 (2001).
18. Brinkman, A. C. *et al.* First Light Measurements of Capella with the Low-Energy Transmission Grating Spectrometer aboard the Chandra X-Ray Observatory. *Astrophys. J.* **530**, L111–L114 (2000).

19. Futamoto, K. *et al.* Detection of Highly Ionized O and Ne Absorption Lines in the X-Ray Spectrum of 4U 1820-303 in the Globular Cluster NGC 6624. *Astrophys. J.* **605**, 793–799 (2004).
20. Masai, K. & Ishida, M. Non-LTE Curves of Growth of X-Ray Absorption Lines. *Astrophys. J.* **607**, 76–83 (2004).
21. Wilms, J., Allen, A. & McCray, R. On the Absorption of X-Rays in the Interstellar Medium. *Astrophys. J.* **542**, 914–924 (2000).
22. Ho, W. G. C., Potekhin, A. Y. & Chabrier, G. Model X-Ray Spectra of Magnetic Neutron Stars with Hydrogen Atmospheres. *Astrophys. J. Supp.* **178**, 102–109 (2008).
23. Hambaryan, V. *et al.* XMM-Newton RGS spectrum of RX J0720.4-3125: an absorption feature at 0.57 keV. *Astron. Astrophys.* **497**, L9–L12 (2009).
24. van Kerkwijk, M. H. *et al.* A Strong, Broad Absorption Feature in the X-Ray Spectrum of the Nearby Neutron Star RX J1605.3+3249. *Astrophys. J.* **608**, 432–443 (2004).
25. Pires, A. M. *et al.* A deep XMM-Newton look on the thermally emitting isolated neutron star RX J1605.3+3249. *Astron. Astrophys.* **623**, A17 (2019).
26. Malacaria, C. *et al.* A Joint NICER and XMM-Newton View of the Magnificent Thermally Emitting X-Ray Isolated Neutron Star RX J1605.3+3249. *Astrophys. J.* **880**, 74 (2019).
27. Borghese, A. *et al.* Discovery of a Strongly Phase-variable Spectral Feature in the Isolated Neutron Star RX J0720.4-3125. *Astrophys. J.* **807**, L20 (2015).
28. Hambaryan, V. *et al.* Phase-resolved spectroscopic study of the isolated neutron star RBS 1223 (1RXS J130848.6+212708). *Astron. Astrophys.* **534**, A74 (2011).

29. Hambaryan, V. *et al.* The compactness of the isolated neutron star RX J0720.4–3125. *Astron. Astrophys.* **601**, A108 (2017).

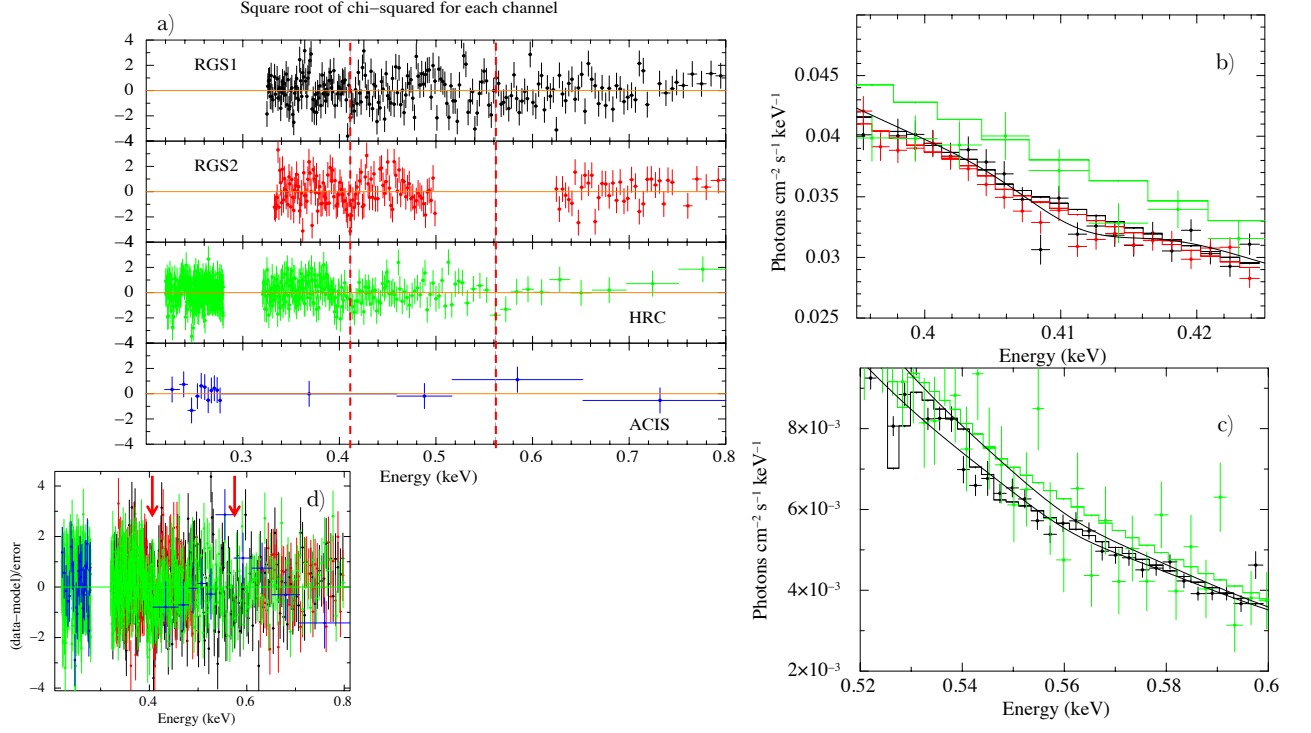


Figure 1: **Lines significance for the high resolution spectra fit.** Panel *a)* shows the $\Delta\chi$ residuals with respect to an absorbed double blackbody model. From top to bottom the sub-panels refer to *XMM-Newton* RGS1 (black), RGS2 (red), *Chandra* LETG-HRC (green), and LETG-ACIS-S (blue), respectively. Vertical dashed red lines indicate the observed energy of the two absorption lines. Panels *b)* and *c)* show a zoom in of the two spectral line regions. In panels *b)* and *c)* RGS1, RGS2, and LETG-HRC data are shown in black, red and green, respectively. Data are signed with a filled dot, the model with no line features as a stepped line. The continuous line in panel *b)* shows the fit to RGS1 and RGS2 data. In panel *c)*, the two continuous lines shows the fit to the RGS1 and LETG-HRC data. Panel *d)* shows the overall $\Delta\chi$ residuals with the position of the two lines marked with an arrow.

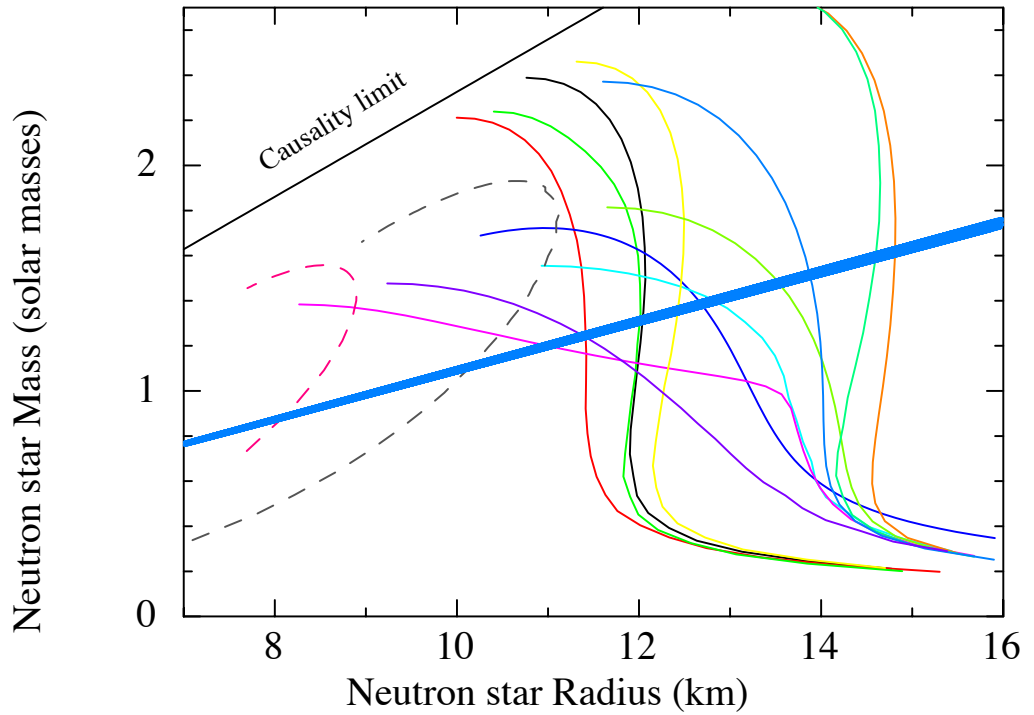


Figure 2: **Constraints from the redshifted absorption lines.** Different neutron star equations of state in the mass-radius plane. The upper left triangle defined by a black straight line is excluded by causality arguments. The two leftmost dashed curves are for strange neutron stars. The constraint from the two redshifted absorption lines is shown with a light blue solid region.

Methods

Data preparation We collected 42 *XMM-Newton* observations (see Table S1). We processed all of them following the analysis threads on the *XMM-Newton* Standard Analysis Software (SAS) pages¹. We used SAS 18.0.0 and the latest available calibrations. We filtered the soft proton flare background using a threshold on (standard) rate of $0.2 \text{ counts s}^{-1}$, computed on the RGS1 data. Background and response matrices were also generated. All spectra were then visually inspected and summed on an instrument basis, together with background and response, using `rgscombine`. We end up with 2.31 Ms (2.24 Ms) for the RGS1 (RGS2), summing 383,021 (325,078) counts in the 0.324–0.8 keV (0.332–0.5 plus 0.625–0.8 keV, due to the failure of one CCD) energy range. Second order spectra are background-dominated ($\sim 8\%$ of source photons) and were discarded. We decided to limit the spectra to 0.8 keV not to encounter problems with the background and because beyond this energy, the number of photons starts becoming too low to search for narrow features. Data were binned to 10 counts per energy bin, given the large number of photons and the relatively low background (82%). A Churazov weighting scheme has been adopted in `XSPEC` (12.10.1f) to ensure χ^2 statistics³².

Simultaneously, we processed the pn data taking the (standard) threshold on rate of $0.4 \text{ counts s}^{-1}$, to filter out soft background flares (being the pn more sensitive than the MOS CCDs working in the RGS, we adopted this more restrictive filtering). All pn observations were collected in small window mode, apart from 4 observations during which the pn was not working or in timing mode. Spectra were extracted from a 880 pixel radius centred on source. Background spectra were extracted from a 600 pixel circular region at the edge of the small window. Single and double events were retained and `FLAG==0` was applied. Ancillary

¹<https://www.cosmos.esa.int/web/xmm-newton/sas-threads>

OBSID	Start Date	RGS GTI	Mode pn	RAWX	RAWY	pn GTI
	YYYY-MM-DD HH:MM:SS	(ks)		(pixel)	(pixel)	(s)
A						
0106260101	2002-04-08 15:59:29	57.3	SMALL	37.0	191.6	57.1
0165971901	2005-03-23 08:28:42	35.3	SMALL	36.1	191.4	34.7
0165972101	2006-03-26 15:34:31	69.8	SMALL	36.9	191.4	69.5
0412600201	2007-03-14 20:00:56	60.1	SMALL	37.0	192.1	65.9
0412600401	2008-03-13 15:46:02	64.4	SMALL	36.8	192.4	63.5
0412600701	2009-03-19 21:23:59	68.7	SMALL	36.1	192.3	68.4
0412600901	2010-03-22 02:44:20	73.6	SMALL	36.8	191.8	73.3
0412601101	2010-09-28 22:52:01	68.3	SMALL	35.9	191.3	68.8
B						
0165971601	2004-09-24 01:36:06	33.3	SMALL	38.4	190.0	33.0
0165972001	2005-09-24 07:52:08	33.5	SMALL	38.3	190.0	33.2
0412600101	2006-10-24 00:27:51	72.8	SMALL	38.1	190.0	72.5
0412600301	2007-10-04 05:42:44	22.2	SMALL	38.3	189.8	38.1
0412600601	2008-10-04 23:21:50	65.0	SMALL	38.5	189.5	62.5
0412600801	2009-10-07 12:01:04	76.0	SMALL	38.0	189.5	76.0
C						
0412601301	2011-03-14 00:41:45	78.2	SMALL	36.5	180.0	82.5
0412601401	2012-04-13 07:06:29	58.9	SMALL	36.3	179.8	66.7
0727760201	2014-03-26 05:36:59	72.6	SMALL	36.3	179.8	73.5
0727760401	2015-03-12 11:22:59	73.2	SMALL	35.5	179.8	74.0
0727760601	2016-03-11 21:28:32	60.5	SMALL	36.0	180.4	76.5
0727761101	2017-03-15 06:22:17	68.8	SMALL	35.5	180.0	69.4
0727761301	2018-04-10 11:52:06	67.5	SMALL	35.0	180.0	68.5
D						
0412602301	2012-09-20 11:17:12	78.3	SMALL	40.0	188.5	80.1
0727760101	2013-09-14 13:57:30	69.8 ₁₄	SMALL	39.6	187.8	70.9
0727760301	2014-09-18 10:40:21	78.7	SMALL	39.9	187.6	78.5
0727760501	2015-10-03 15:33:10	73.4	SMALL	39.4	188.0	81.5
0727761001	2016-09-22 23:51:43	70.4	SMALL	39.8	188.0	70.2

OBSID	Start Date	Exposure
HRC-S	YYYY-MM-DD HH:MM:SS	(ks)
113	2000-03-10 07:54:08	55.1
3380	2001-10-10 05:05:24	164.7
3381	2001-10-12 19:18:22	169.3
3382	2001-10-08 08:17:45	97.7
14418	2013-10-01 05:02:27	29.6
15293	2013-06-12 14:28:42	91.2
ACIS-S		
13198	2011-06-10 07:15:48	28.4
14267	2012-08-03 17:50:18	28.4
15474	2013-07-30 01:39:38	11.7
16265	2013-08-25 11:36:24	16.1
16422	2014-09-29 05:53:10	26.0
17394	2015-06-05 11:18:11	29.1
18416	2016-06-08 03:37:59	28.8
19848	2017-08-03 23:22:46	28.4
20718	2018-07-23 14:19:26	28.2
21809	2019-07-25 13:48:56	26.5

Table S2: **Log of *Chandra* observations.** All ACIS-S observations were taken in FAINT data mode and in Time Exposed (TE) mode.

and response files were generated using `arfgen` and `rmfgen` and the latest calibration files. Following Sartore et al.¹⁶, we sum pn spectra on a detector position basis. We individuated five groups of positions (see Table S1). We collected 5.1 Mcounts in 2.0 Ms in the 0.2–0.8 keV energy range. Data were binned to 25 counts per energy bin. A few observations did not find a suitable group to join (thus having a small statistics) and were discarded.

For the *Chandra* data, we used CIAO v.4.12 and CALDB 4.9.1. We reprocess all the public data with `chandra_repro` and follow the analysis threads². We collected data for 0.61 Ms for the HRC (6 observations) and 0.25 Ms for the ACIS (10 observations, see Table S2). Only first order data (plus and minus) were considered and summed up. We restricted the energy range of the LETG-HRC to 0.22–0.28 keV plus 0.32–0.8 keV to get rid of the effective area decrease around the carbon edge. The total number of collected counts is 0.18 Mcounts. For the LETG-HRC the background (68% of the total) and the spectral resolution are high, so that we binned the data to 300 counts per energy bin. LETG-ACIS data can be used only when the ACIS-S is on the grating path, due to its higher sensitivity to soft photons. We restricted the energy range to 0.22–0.28 keV and 0.41–0.8 keV, where we collected 6 kcounts, mainly in the very soft part of the spectrum. Data were binned to 150 counts per energy bin.

Before starting with the line fitting procedure, we fit the single spectra binned to one photon per energy channel (and adopting the Cash statistics) with a double blackbody model. We then add a Gaussian single line with width (σ) fixed to 0.5 eV. This line was then left free to vary across the entire spectrum (0.2–0.8 keV) to get rid of single channels, coincident with hot pixels or mis-calibrated channels.

²https://cxc.cfa.harvard.edu/ciao/threads/spectra_letghrcs/

Line search: observer-frame lines After grouping and filtering we started with the search for a meaningful continuum model over which search for spectral features. Spectral fits were carried out with the spectral package XSPEC³⁰. After some attempts, we considered a model made by two blackbody spectra (one soft and one harder) absorbed by a column density. The fit is equivalent to the one that we can obtain from an absorbed blackbody plus a neutron star atmosphere model, but it is faster in the computation (being analytical and not relying on interpolations). The absorbing column density has been modelled with `tbabs`²¹, using Verner cross-sections³¹ and `wilm` abundances. Given the large number of counts and small intercalibration uncertainties, we leave free all the parameters for each instrument. The blackbody radius has been limited to 20 km and the distance fixed to 120 pc. Only for the fit of LETG-ACIS data the soft blackbody component is unconstrained. The results of the fit are reported in Table S3. The overall fit provided a reduced $\chi_r^2 = 1.23$ for 949 degrees of freedom (dof) and a corresponding null hypothesis probability (nhp) of 8×10^{-7} .

Instrument	N_H (10^{20} cm^{-2})	Blackbody1 kT (eV)	Normalisation1 (10^5)	Blackbody2 kT (eV)	Normalisation2 (10^8)
RGS1	5.0 ± 1.0	60.5 ± 0.6	2.6 ± 0.4	26.6 ± 1.0	$2.9_{-1.5}^{+2.3}$
RGS2	4.6 ± 1.6	60.2 ± 0.8	2.6 ± 0.6	25.6 ± 1.2	$4.2_{-2.2}^{+4.2}$
HRC	1.5 ± 0.3	60.2 ± 0.9	2.3 ± 0.3	14.1 ± 5.1	> 2.2
ACIS-S	0.5 ± 0.3	67.7 ± 1.8	0.8 ± 0.2	–	–

Table S3: **Fit with an absorbed double blackbody model.** Errors were computed with $\Delta\chi^2 = 2.71$. The normalisation K is related to the equivalent emitting radius R by the relation $K = (R/10\text{km})^2/(d/10\text{kpc})^2$, with d the source distance, 120 pc.

We also tried the more complex *tbnew* absorption model. We tried to leave free all the

element abundances, but only N and O were significantly different from 1. Leaving free the abundances of these two elements, we obtained an improvement in the fit of $\Delta\chi^2 = 17.5$ (and a $\chi^2_{\text{r}} = 1.22$ for 946 degrees of freedom). The abundances with respect to the solar values are $[\text{N}/\text{N}_{\odot}] = 6.0^{+4.1}_{-2.7}$ and $[\text{O}/\text{O}_{\odot}] = 2.5^{+1.7}_{-0.9}$. These abundances are much higher than solar and are not easily interpretable. In addition, the fit is still not statistically acceptable.

We then started the iteration process adding a Gaussian line (using `tbabs` to model interstellar absorption). The line was kept free to vary in the 0.25–0.8 keV energy range, with a free Gaussian width in the 1–100 eV range. We decided to stop when the the improvement in the χ^2 for the addition of a new line is less than 10. After a first fit, a search of the best fit line energy is obtained performing a `steppar` search with 1199 or 1201 steps (i.e. ~ 0.5 eV) resolution. The variation of the χ^2 is annotated (see Table S4) and all the line parameters are left free to vary when we include a further line. As a visual impression, in Fig. S1 we show the improvement in the χ^2 as a function of energy depending on three fixed line widths (in the fit the line width is left free to vary).

We also report in Table S4 the χ^2 variation on an instrument basis. We report in Table S5 the final line values. The addition of a further line produces a $\Delta\chi^2 = 2.3$ and we deemed it a statistical fluctuation. This putative line has an energy close to the centroid of Line2 and has a line width that saturates our limit of 100 eV. It is apparent from the values in the upper part of Table S4 that Line1 and Line3 are very close (and consistent in energy) and that RGS1 and RGS2 react in different ways to the inclusion of this line. We therefore restart the process including a line close to 410 eV made by the superposition of two Gaussians, one narrow and one large. Fits are reported in the the bottom part of Table S5. Each line normalisation is

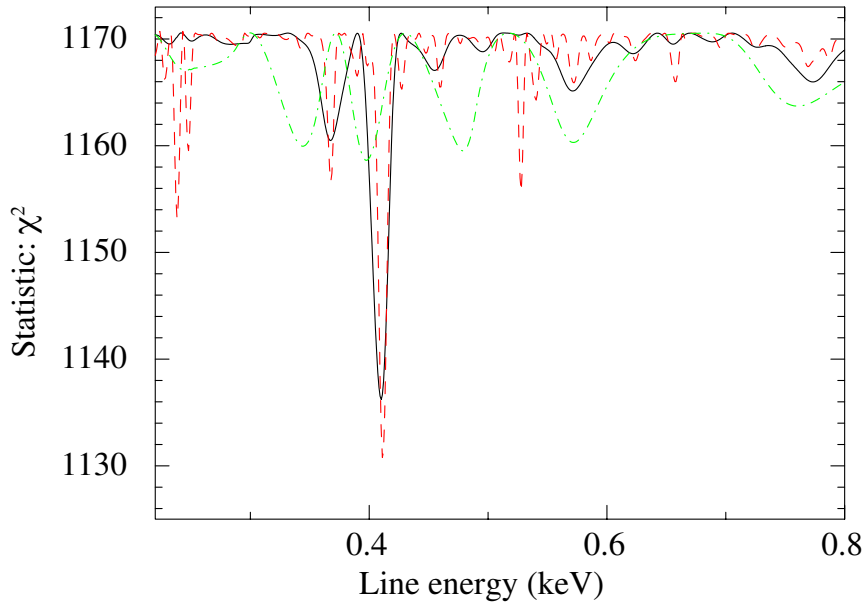


Figure S1: **Improvement in the χ^2 of high resolution spectra for the inclusion of a Gaussian line feature.** We show the decrease of the χ^2 as a function of energy for the inclusion of a fixed-width Gaussian line. This has been obtained adding a line and then computing the improvement with the `steppar` command within XSPEC. The continuous (black) curve refers to a 10 eV line width, the dashed (red) curve to a 3 eV line width, and the dot-dashed (green) curve to a 30 eV line width, respectively.

different from zero at $> 3.5\sigma$ confidence level. The overall fit is reported in Table S5. The $\chi^2 = 1093.7$ for 941 dof ($\chi_r^2 = 1.17$). The fit can be appreciated in Fig. S2.

	Starting χ^2	$\Delta\chi^2$	RGS1	RGS2	HRC	ACIS
Line1 411 eV N	1170.6	43.4	10.7	27.0	5.5	(2.0)
Line2 569 eV	1127.1	17.5	18.2	(1.0)	3.3	-4.1
Line3 416 eV L	1109.7	16.4	19.7	-8.2	4.8	(-0.9)
Line1 411 eV N+L	1170.6	46.6	12.3	26.1	7.8	(0.4)
Line2 561 eV	1123.9	37.2	35.6	(1.3)	5.5	-5.2

Table S4: χ^2 variations for the inclusion of lines. Values in parenthesis indicate that the added line centroid is outside the noted energy range: the best fit changes because response matrices are not diagonal. A negative value indicates a worsening of the fit due to the line inclusion.

Line search: redshifted lines We searched for redshifted lines. We considered NVII Ly α at 500.3 eV and OVIII Ly α at 653.6 eV as the two candidates. These lines were identified following an iterative process with the main lines (C, N, O and Ne) to identify which can be coupled to a common redshift. We then fit the data using a redshifted Gaussian `zgaus` instead of a Gaussian, keeping the structured line for NVII Ly α . In addition, we impose the same line width to the two wide lines. Given the smaller degrees of freedom we expect a slightly worse fit with respect to the unredshifted lines. We obtain a $\chi^2 = 1103.8$ for 943 dof ($\chi_r^2 = 1.17$). Leaving free the two line widths improves the χ^2 by 6.4, resulting in a probability of chance coincidence by means of an F-test of 11.6%. If we instead leave the two redshifts independent, the χ^2 improves by 9.7, with an F-test probability of 1.9%. Fit parameters are reported in Table S6. Line equivalent widths increase due to the redshift. Based on Futamoto et al.¹⁹ and assuming a thermal limit of 10^6 K, we can derive a column density of $N_{\text{OVIII}} \sim 4 \times 10^{20} \text{ cm}^{-2}$

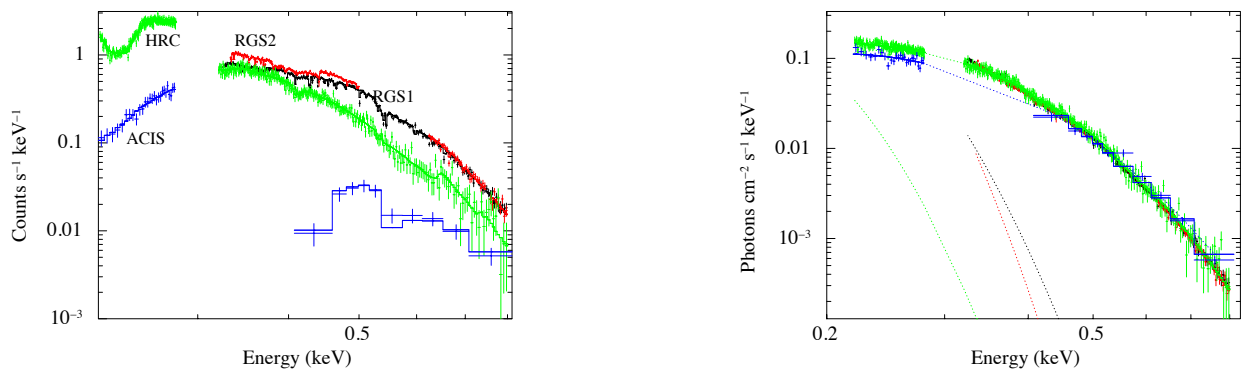


Figure S2: **High resolution spectra of RXJ1856.** In the left panel are shown the four high resolution spectra of RXJ1856 fitted with an absorbed double blackbody model and two Gaussian lines (one with structure) as discussed in the text. From top to bottom the spectra refer to *XMM-Newton* RGS1, RGS2, *Chandra* LETG-HRC, and LETG-ACIS-S, respectively. In the right panel the unfolded spectra are shown with the same color coding. Dotted lines are for the two blackbody model components.

Instrument	N_H (10^{19} cm^{-2})	Blackbody1 kT (eV)	Normalisation1 (10^5)	Blackbody2 kT (eV)	Normalisation2 (10^8)
RGS1	$6.5^{+9.9}_{-5.6}$	62.0 ± 0.7	1.6 ± 0.3	22.0 ± 5.7	$3.8^{+78.4}_{-3.2}$
RGS2	$3.3^{+9.4*}_{-3.3}$	61.8 ± 1.0	1.6 ± 0.4	16.9 ± 4.9	> 2.7
HRC	$16.1^{+4.5}_{-2.8}$	60.3 ± 1.0	2.4 ± 0.4	16.1 ± 3.3	> 2.0
ACIS-S	$6.0^{+3.4}_{-3.1}$	67.6 ± 1.7	0.8 ± 0.2	–	–

Line	Energy (eV)	Width (σ) (eV)	Equivalent Width (eV)
Line N	–	3.9 ± 1.6	0.64 ± 0.23
Line L	–	37.6 ± 10.0	$3.5^{+2.2}_{-2.3}$
Line N+L	411.3 ± 1.3	–	4.2 ± 2.3
Line2	561.5 ± 10.0	31.7 ± 11.8	$6.5^{+2.2}_{-2.3}$

Table S5: **Fit with an absorbed double blackbody model and lines.** Errors were computed with $\Delta\chi^2 = 2.71$, or 90% confidence level for one parameter of interest. The normalisation K is related to the equivalent emitting radius R by the relation $K = (R/10\text{km})^2/(d/10\text{kpc})^2$, with d the source distance, 120 pc. A * close to one parameter means that it is consistent with zero. The equivalent widths refer to RGS1.

and $N_{\text{NVII}} \sim 2 \times 10^{20} \text{ cm}^{-2}$. If distributed isotropically in the neutron star atmosphere this give $\sim 2 \times 10^{11} \text{ g}$ of OVIII and $\sim 10^{11} \text{ g}$ of NVII, assuming 12 km radius and 1 cm thickness.

While there is a desert of strong high-ionisation lines around the energy of the N VII Ly α , this is not the case for the OVIII Ly α . One can in principle envisage that the line identification is not correct and this second line might be attributed to OVII Ly β (at 665.6 eV), or even to OVII Ly γ (at 697.8 eV). We first fix the line energy of the second line to OVII Ly β (at 665.6 eV). The fit improves to $\chi^2 = 1095.0$ for a $\Delta\chi^2 = 8.9$. Based on the Akaike information criterion ($AIC = 2k + \chi^2$, where k is the number of parameters³³), the OVII Ly β improves the fit at a significance level of (equivalent) 2.5 Gaussian σ . We also left free the energy of this second line as well as the redshift and anchor the fit to the N VII Ly α . In this case the line energy ends at $667_{-11}^{+16} \text{ eV}$, in between OVII Ly β and OVII Ly γ . Based on the AIC criterion, the fit improves by 2.6 Gaussian σ . Independently on the line identification, as a result of these experiments the gravitational redshift move to 0.217 ± 0.004 , with a mere 0.5% change.

Line search: pn detector As shown by Sartore et al.¹⁶, the spectrum of RXJ1856 on the pn detector is position dependent. This is mainly due to the huge number of counts coupled to small calibration uncertainties. We identified five groups of positions (see Table S1, A to E). Data were grouped on a position basis and spectra were independently fitted with the absorbed double blackbody model, adding 0.5% systematic error and allowing for a 20 km neutron star maximum radius. For four of the spectra the second blackbody component was not needed (group C needed it). The column densities range from (0.3 ± 0.1) to $(0.9 \pm 0.6) \times 10^{20} \text{ cm}^{-2}$ and the blackbody temperature 61.3 ± 0.1 to $63.4 \pm 0.1 \text{ eV}$. The overall spectrum provides a reduced $\chi_r^2 = 1.68$ for 552 dof. Residuals are shown in Fig. S3. We iteratively add lines, as

Instrument	N_H (10^{19} cm^{-2})	Blackbody1 kT (eV)	Normalisation1 (10^5)	Blackbody2 kT (eV)	Normalisation2 (10^8)
RGS1	$17.8^{+13.3}_{-8.2}$	60.6 ± 0.8	2.2 ± 0.5	20.1 ± 4.9	$26.9^{+137.8}_{-24.8}$
RGS2	$16.7^{+10.5}_{-8.0}$	60.3 ± 0.9	2.3 ± 0.5	17.6 ± 4.1	> 12.6
HRC	$20.1^{+6.0}_{-4.4}$	59.9 ± 1.1	2.7 ± 0.6	18.7 ± 4.1	$4.7^{+46.7}_{-3.0}$
ACIS-S	$13.1^{+2.6}_{-2.3}$	65.4 ± 1.4	1.2 ± 0.3	–	–

Line	Common Redshift	Width (σ) (eV)	Equivalent Width (eV)
NVII N	–	$4.9^{+2.1}_{-1.4}$	0.65 ± 0.24
NVII L	–	$54.6^{+6.8}_{-5.7}$	7.1 ± 2.3
NVII N+L	0.216 ± 0.004	–	7.8 ± 2.3
OVIII	–	$54.6^{+6.8}_{-5.5}$	8.8 ± 2.5

Table S6: **Fit with an absorbed double blackbody model and redshifted lines of high resolution spectral data.** Errors were computed with $\Delta\chi^2 = 2.71$, or 90% confidence level for one parameter of interest. The normalisation K is related to the equivalent emitting radius R by the relation $K = (R/10\text{km})^2/(d/10\text{kpc})^2$, with d the source distance, 120 pc. The equivalent widths refer to RGS1.

done for the high resolution spectra.

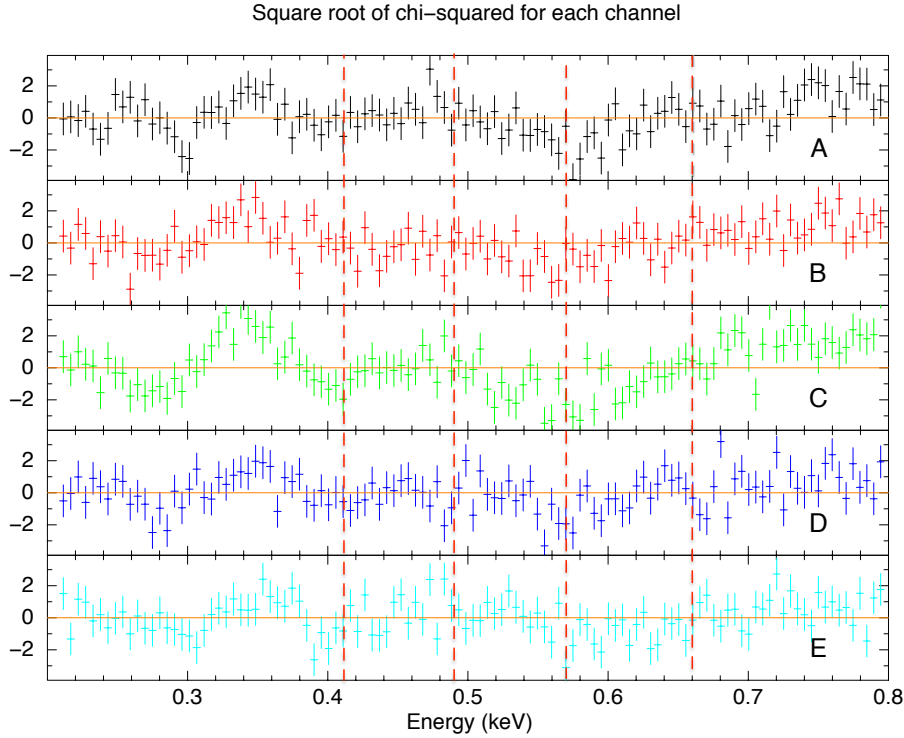


Figure S3: **Delta χ^2 contributions for the five *XMM-Newton* position-dependent pn spectra.**

The five panels show the $\Delta\chi^2$ residuals with respect to an absorbed double blackbody model for spectra of groups A to E, respectively. Vertical dashed red lines indicate the observed energy of the four tentative absorption lines.

We report below the final line values, because these values change as the fit procedure proceeds. The line width has been kept tied among all the lines. We decided to stop the line inclusion process when the improvement in the χ^2 falls below 10. The first line to be found is one at 411.5 ± 3.6 eV, width 22_{-5}^{+4} eV, and the equivalent width of 15.8 ± 1.2 eV. The variation in the χ^2 is $\Delta\chi^2 = 252.8$. The second line is at 661.1 ± 8.5 eV and the equivalent width of 12.2 ± 1.5 eV. The improvement of the fit provides $\Delta\chi^2 = 88.9$. A third significant line is present in the overall pn spectrum at 490.1 ± 5.4 eV and the equivalent width of 17.1 ± 1.2 eV.

The variation in the χ^2 is $\Delta\chi^2 = 54.5$. The fourth line is at 570.2 ± 7.1 eV and the equivalent width of 17.4 ± 1.8 eV. The variation in the χ^2 is $\Delta\chi^2 = 25.6$. The overall fit is presented in Fig. S4 and line energies are reported in Table S7. A further addition improves the χ^2 by 7.1 and we decided not to consider it. At the end of the process also the second blackbody component turned out to be important in the fit and the column density is in line with the high resolution fit.

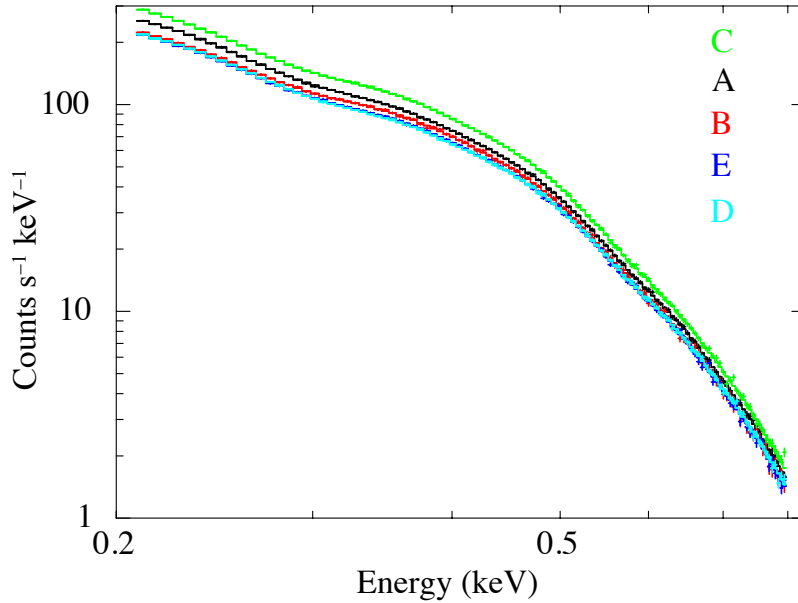


Figure S4: *XMM-Newton* **pn spectra of RXJ1856**. The five position-dependent pn spectra of RXJ1856 fitted with an absorbed double blackbody model and four Gaussian lines, as discussed in the text.

The lines at 411.5 eV and 570.2 eV can be identified with the lines found in the high

resolution spectral data. The other two lines found in the on analysis did not pass our threshold during the analysis of high resolution data. We go back to the RGS and LETG data to derive an upper limit for the lines at 661.1 eV and 490.1 eV. The inclusion of the first (fixed energy) line provides a $\Delta\chi^2 = 7.1$ and the upper limit on the equivalent width is < 12.9 eV. The inclusion of the second line provides a $\Delta\chi^2 = 4.6$ and the upper limit on the equivalent width is < 14.8 eV. Both equivalent widths are slightly smaller than the values derived from the pn data.

As before, these lines can be tentatively identified as NV Ly α (412 ± 4 eV vs. 421.5 eV), NVII Ly α (490 ± 5 eV vs. 500.3 eV), OVII Ly α (570 ± 7 eV vs. 574.0 eV), and OVIII Ly β (661 ± 9 eV vs. 665.6 eV), respectively, even if the dependence on position of the pn spectral response, make us not fully trust the pn spectra. As discussed before, however, the line equivalent widths are too intense to come from the interstellar medium and the Nitrogen lines require the same (small, $z \sim 0.02$) redshift, which is not requested by Oxygen lines. As above, we are forced to look for gravitationally redshifted lines.

Given the high temperature of the neutron star atmosphere, we were driven in our choice by the lowest level of the highest ionisation level species. Tentatively, we identify the lines with NVII Ly α (the line with observed energy at 412 eV), OVII Ly α (490 eV), OVIII Ly α (570 eV), and OVIII Ly β (662 eV). The overall fit is good with a reduced $\chi^2 = 0.97$ with 544 dof (67% nhp). The line width is 46 ± 5 eV. The equivalent widths are 18.7 ± 10.6 eV (NVII Ly α), 9.0 ± 4.2 eV (NVII Ly β), 16.8 ± 4.1 eV (OVIII Ly α), and 13.7 ± 8.2 eV (OVIII Ly β). The gravitational redshift is $z_g = 0.224 \pm 0.015$. This value is consistent with the one derived from high resolution spectral data. Given the uncertainties in the position-dependent calibration of the pn detector, we consider this as an indirect confirmation of the results obtained with high

resolution spectral data.

Line energy (eV)	Rest-frame line (eV)	Redshifted identified line (eV)	Projected rest-frame line energy (eV) [†]
411.5 ± 3.6	NV Ly α (421.5*)	NVII Ly α (500.3 eV)	497^{+17}_{-13}
490.1 ± 5.4	NVII Ly α (500.3*)	NVII Ly β (593.0 eV)	592^{+21}_{-16}
570.2 ± 7.1	OVI Ly α (574.0)	OVI Ly α (653.6 eV*)	689^{+26}_{-19}
661.1 ± 8.5	OVI Ly β (665.6)	OVI Ly β (774.6 eV)	799^{+30}_{-24}

*marks line energies that are not consistent within the errors with the observed values.

[†] These energies were computed leaving free the redshift within the 3σ confidence interval (0.188 – 0.234) and then leaving all the line energies free.

Table S7: Significant lines discovered in the pn data and tentative identifications. Line energy errors were computed with $\Delta\chi^2 = 2.71$, or 90% confidence level for one parameter of interest.

Given that data were collected over several years, the timing solution is not good enough to afford a pulse phase spectroscopy study.

MOS data were all taken in timing mode and the usable energy range starts from ~ 0.5 keV. For this reason MOS data were not considered here.

Line search: tentative physical modelling We also tried a physical modelling of the absorber using *XSTAR*. *XSTAR* is used for calculating the physical conditions and emission/absorption spectra of photoionised gases³⁴. We used the analytical version of *XSTAR*, i.e. *warmabs* (v.2.2, ³⁵). We adopted the highest population for a density of 10^{16} g cm⁻³. Modelling the

neutron star atmosphere is beyond the scope of this paper, so we approached the fit with this model having clear in mind that this cannot provide a completely satisfactory description of the absorber. After a first fitting run, it became clear that the hot column density is tightly coupled with the Oxygen and Nitrogen abundances, so we fixed it to its highest value, 10^{24} cm^{-2} .

The overall fit is better than the one with an absorbed double blackbody model but worse than the one obtained with the addition of three Gaussian lines, as expected being the grid not able to perfectly model the large line widths, even if leaving free the turbulent velocity parameter improves the fit considerably. The fit values are reported in Table S8. The χ^2 is 1128.1 for 943 dof ($\chi_r^2 = 1.20$). The logarithm of the ionisation parameter $\xi = L/(nr^2)$ (where L is the ionising luminosity, r is the distance, and n is the particle density) is high with a lower limit of 1.6 (90% confidence). The abundances of all elements but Nitrogen and Oxygen are consistent with zero, thus we fixed all of them to zero. The column density of Oxygen is unconstrained. Apart from the interstellar lines, the two strongest absorption lines are NVII Ly α and OVIII Ly α . Weaker lines are, among others, from OVIII Ly β , NVII Ly β , NVI Ly α . The redshift is 0.214 ± 0.004 , consistent with the one derived with the Gaussian lines fit.

30. Arnaud, K. E. XSPEC and PyXSPEC. *AAS HEAD meeting* **15**, 115.02 (2016).
31. Verner, D. A. *et al.* Atomic Data for Astrophysics. II. New Analytic FITS for Photoionization Cross Sections of Atoms and Ions. *Astrophys. J.* **465**, 487–498 (1996).
32. Churazov, E. *et al.* Mapping the Gas Temperature Distribution in Extended X-Ray Sources and Spectral Analysis in the Case of Low Statistics: Application to ASCA Observations of

Instrument	ISM N_H (10^{20} cm^{-2})	Blackbody1 kT (eV)	Blackbody2 kT (eV)
RGS1	4.6 ± 1.1	60.5 ± 0.6	26.9 ± 1.0
RGS2	2.5 ± 1.9	61.1 ± 0.9	25.1 ± 1.6
HRC	1.4 ± 0.5	60.2 ± 0.9	14.6 ± 4.6
ACIS-S	0.4 ± 0.3	67.7 ± 1.8	–
ξ	$2^* (> 1.6)$		
Hot N_N (10^{17} cm^{-2})	1.3 ± 0.4		
Hot N_O (10^{17} cm^{-2})	$0.6^* (< 1.1)$		
Turbulent velocity (10^8 cm s^{-1})	$3.7_{-1.0}^{+1.5}$		
Redshift (z)	0.214 ± 0.004		

Table S8: **Fit with an absorbed double blackbody model and hot absorbing medium.** Errors were computed with $\Delta\chi^2 = 2.71$, or 90% confidence level for one parameter of interest. A * indicates a parameter whose error is not constrained: we reported the value of the fit and the lower limit in parenthesis.

Clusters of Galaxies. *Astrophys. J.* **471**, 673–682 (1996).

33. Arcodia, R. *et al.* X-ray absorption towards high-redshift sources: probing the intergalactic medium with blazars. *Astron. Astrophys.* **616**, A170 (2018).
34. Kallman, T. & Bautista M. Photoionization and High-Density Gas. *Astrophys. J. Supp.* **133**, 221–253 (2001).
35. Gatzuz, E. *et al.* Photoionization Modeling of Oxygen K Absorption in the Interstellar Medium: The Chandra Grating Spectra of XTE J1817-330. *Astron. Astrophys.* **768**, 60

(2013).

Acknowledgements We thank F. Nicastro for providing the column densities for the ISM lines and V. Braitto for discovering a subtle error in the conversion from Ångstron to keV. We thank V. Braitto, F. Nicastro, G. Ponti, R. Turolla for useful discussions on several aspects of the paper. This work made us of public data from the *XMM-Newton* and *Chandra* satellites. Data were retrieved from the ESA and *Chandra* archives, respectively. This work started as a tool to make Emma work out complicated additions of the observing times. It then evolved into a proper manuscript and I tried to keep alive the interest in STEM disciplines in Marta, telling her about redshifted lines from the neutron star surface. Strange things happen during a long lockdown.

Author Contributions S.C. contributed to the entire paper.

Author information

Competing Interests The authors declare that they have no competing financial interests.

Correspondence Correspondence and requests for materials should be addressed to S.C. (email: sergio.campana@brera.inaf.it)

Reprints Reprints and permissions information is available at www.nature.com/reprints.

Data availability The datasets generated during and/or analysed during this study are available upon request.

Code availability No custom code. XSPEC is freely available as part of `heasoft`. *XMM-Newton* and *Chandra* data reduction software are publicly available, too.

Figures

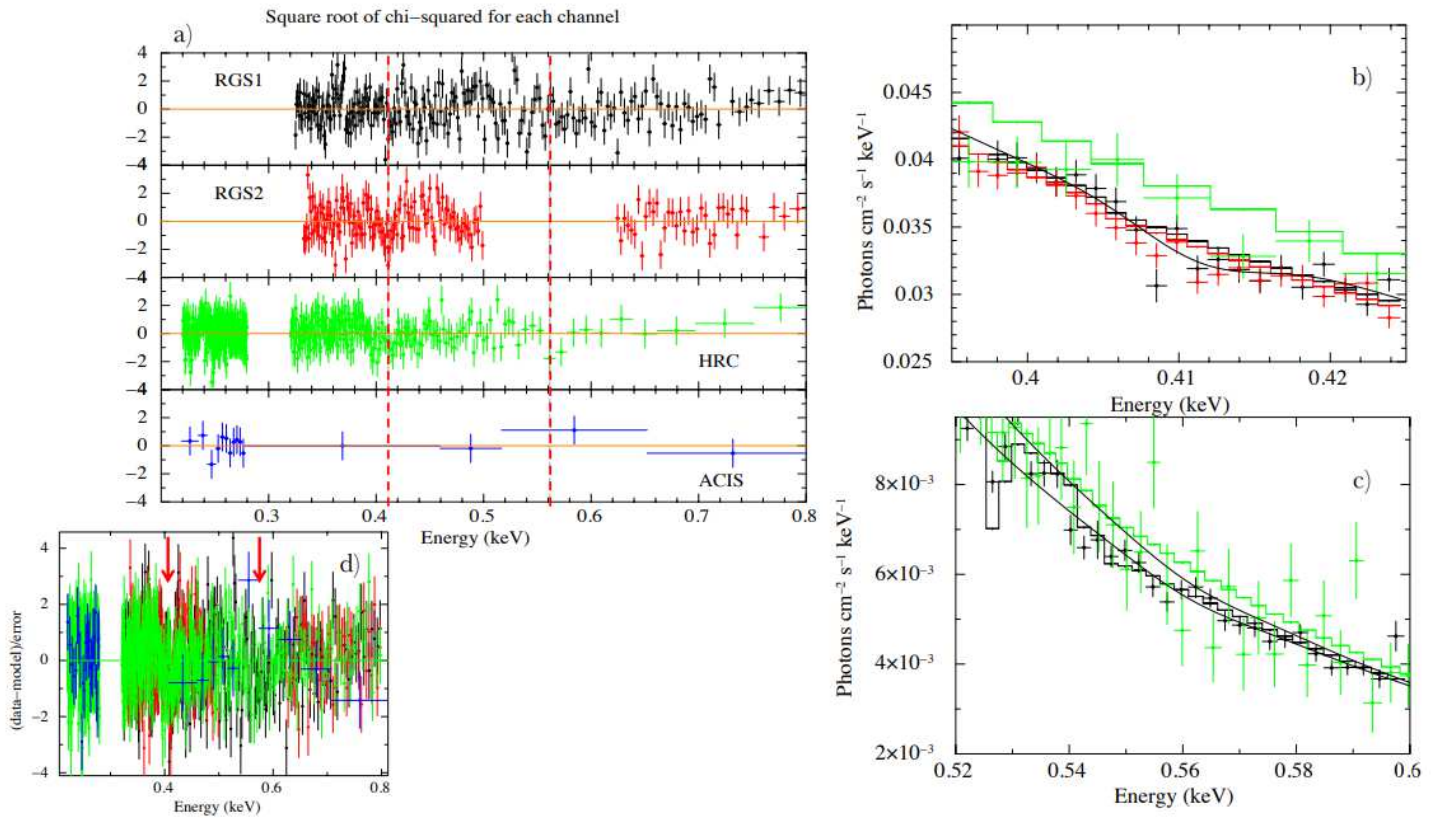


Figure 1

Lines significance for the high resolution spectra fit. Panel a) shows the $\Delta\chi$ residuals with respect to an absorbed double blackbody model. From top to bottom the subpanels refer to XMM-Newton RGS1 (black), RGS2 (red), Chandra LETG-HRC (green), and LETG-ACIS-S (blue), respectively. Vertical dashed red lines indicate the observed energy of the two absorption lines. Panels b) and c) show a zoom in of the two spectral line regions. In panels b) and c) RGS1, RGS2, and LETG-HRC data are shown in black, red and green, respectively. Data are signed with a filled dot, the model with no line features as a stepped line. The continuous line in panel b) shows the fit to RGS1 and RGS2 data. In panel c), the two continuous lines shows the fit to the RGS1 and LETG-HRC data. Panel d) shows the overall $\Delta\chi$ residuals with the position of the two lines marked with an arrow.

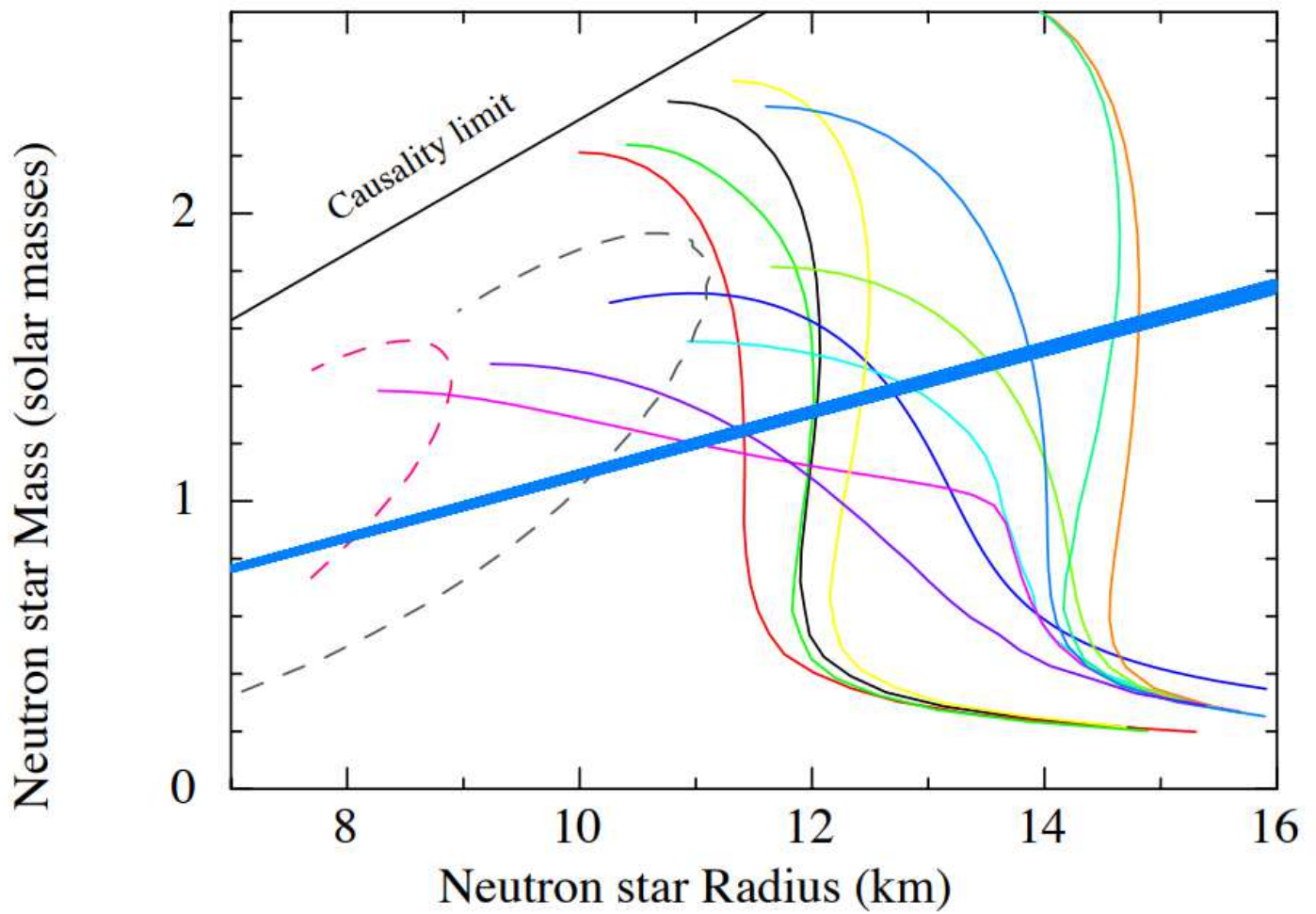


Figure 2

Constraints from the redshifted absorption lines. Different neutron star equations of state in the mass-radius plane. The upper left triangle defined by a black straight line is excluded by causality arguments. The two leftmost dashed curves are for strange neutron stars. The constraint from the two redshifted absorption lines is shown with a light blue solid region.